

3D Printed Tooling for Injection Molded Microfluidics

Neil Convery, Iliyana Samardzhieva, John Moir Stormonth-Darling, Sean Harrison, Gareth J. Sullivan, and Nikolaj Gadegaard*

Microfluidics have been used for several decades to conduct a wide range of research in chemistry and the life sciences. The reduced dimensions of these devices give them advantages over classical analysis techniques such as increased sensitivity, shorter analysis times, and lower reagent consumption. However, current manufacturing processes for microfluidic chips either limit them to materials with unwanted properties, or are not cost-effective for rapid-prototyping approaches. Here the authors show that inlays for injection moulding can be 3D printed, thus reducing the skills, cost, and time required for tool fabrication. They demonstrate the importance of orientation of the part during 3D printing so that features as small as $100 \times 200 \mu\text{m}$ can be printed. They also demonstrate that the 3D printed inlay is durable enough to fabricate at least 500 parts. Furthermore, devices can be designed, manufactured, and tested within one working day. Finally, as demonstrators they design and mould a microfluidic chip to house a plasmonic biosensor as well as a device to house liver organoids showing how such chips can be used in organ-on-a-chip applications. This new fabrication technique bridges the gap between small production and industrial scale manufacturing, while making microfluidics cheaper, and more widely accessible.

1. Introduction

Since its conception, microfluidics has been able to offer an improvement over classical analysis techniques such as genomics,^[1] biochemical assays,^[2] and live cell studies^[3] as well as the study of previously unseen phenomena.^[4–6] Currently, polydimethylsiloxane (PDMS) is still the preferred material for most microfluidics applications in research due to its simple manufacturing process and low cost for small production runs. However, PDMS suffers from drawbacks such as small molecule adsorption,^[7] leaching,^[8] deformation,^[9] hydrophobic recovery,^[10] evaporation,^[11] and low throughput meaning that for it is rarely used in consumer products. For industrial and consumer applications, plastics are widely regarded as the superior material due to their biocompatibility and optical properties.^[12] Furthermore, the majority of cell culture research is conducted on engineering polymers such as polystyrene (PS) meaning

they are well understood materials from a biological perspective.^[13] As such, there has been a great deal of research since the turn of the century in fabricating plastic microfluidic devices using manufacturing methods such as computerized numerical control (CNC) milling,^[14–16] laser milling,^[15,17] micro-machining,^[18] 3D printing,^[19] and hot embossing.^[20–23] However, the widest used plastic fabrication method in industry is injection molding. Injection molding offers high throughput, high replication quality, and low part cost when compared to any other plastic manufacturing process. Through injection molding, $<100 \text{ nm}$ features have been replicated,^[24] however, its use has been hindered by the cost required to process a master structure for all replicas to be molded from. Masters (or inlays as they are referred to here) are fabricated through electroplating of micro-machined silicon,^[25,26] CNC milling,^[27,28] etched quartz,^[29] etched silicon,^[30] polytetrafluoroethylene (PTFE) backed nickel,^[31] SU-8 patterned nickel,^[32] photo curable polyurethane resins,^[33] bulk metallic glasses,^[34] SU-8 on polyamide sheets,^[35] and epoxy resins.^[36] However, despite the variety of inlay production processes available, none offer a low enough cost to be used during the development of a device or for small batch, proof of concept experiments conducted in academic research settings.

To combat these issues, we demonstrate the use of stereolithography (SLA) 3D printed inlays as tooling for injection

N. Convery, I. Samardzhieva, J. M. Stormonth-Darling, N. Gadegaard

Division of Biomedical Engineering

James Watt School of Engineering

University of Glasgow

Glasgow G12 8LT, UK

E-mail: Nikolaj.Gadegaard@glasgow.ac.uk

S. Harrison, G. J. Sullivan

Hybrid Technology Hub—Centre of Excellence

Institute of Basic Medical Sciences

University of Oslo

Oslo 0317, Norway

S. Harrison, G. J. Sullivan

Department of Pediatric Research

Oslo University Hospital


Oslo 0317, Norway

G. J. Sullivan

Institute of Immunology

Oslo University Hospital

Oslo 0317, Norway

 The ORCID identification number(s) for the author(s) of this article can be found under <https://doi.org/10.1002/mame.202100464>

© 2021 The Authors. Macromolecular Materials and Engineering published by Wiley-VCH GmbH. This is an open access article under the terms of the Creative Commons Attribution License, which permits use, distribution and reproduction in any medium, provided the original work is properly cited.

DOI: 10.1002/mame.202100464

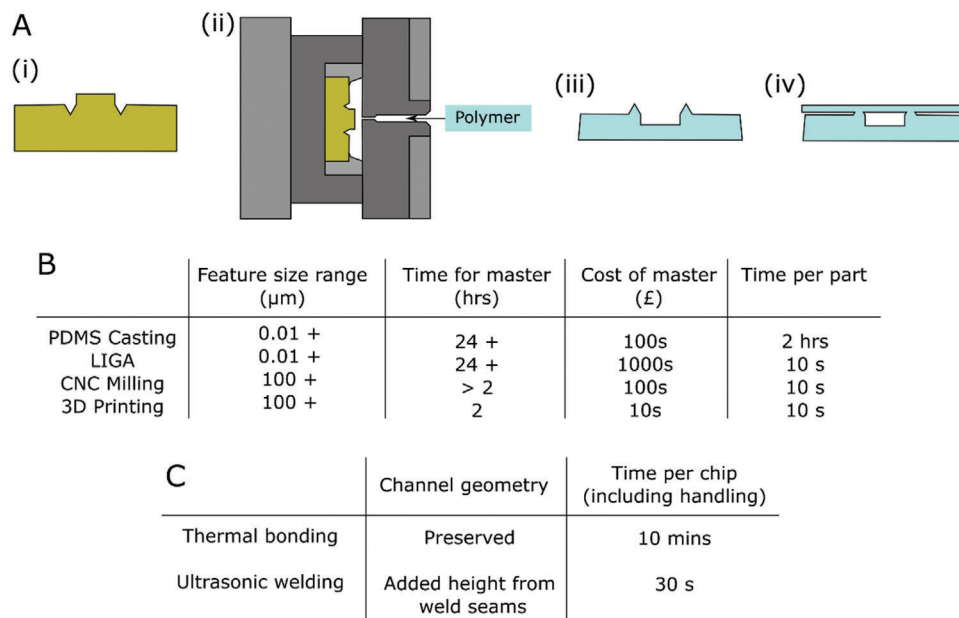


Figure 1. A) shows a cross-sectional schematic the fabrication process of the chips with the 3D printed master (i) and the injection molding process (ii). Once molded, the polymer part (iii) is then sealed through ultrasonic welding to give a complete microchannel (iv). B) shows a comparison between difference fabrication comparing the feature size, time, and cost required for fabrication (LIGA: Lithographie, Galvanoformung, Abformung. C) shows a comparison of commonly used sealing methods comparing the impact on channel geometry and time requirements.

molding using a commercially available, unaltered 3D printer. SLA printing works by curing layers of a photocurable resin in a stepwise manner allowing for a highly customizable, 3D part with low surface roughness and fine feature detail as well as rapid and simple fabrication. 3D printing has widely been used for the direct fabrication of microfluidic devices as it allows designs to be changed and rapidly produced. However, this approach is limited by low-throughput capabilities and the difficulty in upscaling the fabrication process when a final design is settled upon. Although an approach using 3D printed masters for the replica molding of PDMS microfluidic devices has been presented previously,^[37] the translation from PDMS casting, to injection molding represents a significant advancement due to the aforementioned material and high-throughput advantages. We demonstrate that commercially available resin can withstand the high pressures (>800 bar) and temperatures (>250 °C) of a typical injection molding process while simultaneously allowing for accurate fabrication and replication of micro features at a fraction of the cost, time, and expertise of the inlay manufacturing methods listed above. Although ultrasonic welding has been used for the sealing of microfluidic devices in the past,^[38,39] the effect of the dimensions of the weld seams and welding process on the geometry on the microfluidic channel has not been well reported. Here we describe these details for weld seams with dimensions relevant to the 3D printing process so that a reliable seal with minimal effect of the channel shape can be achieved. The molding and sealing process is shown in **Figure 1A**. Furthermore, the use of a 3D printed inlay provides a link between the rapid prototyping preferred in microfluidics research and high throughput, industrial scale manufacture—an important feature of product development where identifying and optimizing the final, mass production process of a device as early as possible is highly desirable.^[12]

Finally, 3D printing allows for the realization of features that would otherwise be difficult to manufacture by traditional methods. For example, we were able to manufacture inlays containing not only micro-channels, but also the weld seams required for ultrasonic welding to seal the devices in a rapid manner. These 300 × 300 μm triangular prisms round the edge of the channels are very difficult to fabricate in silicon and by CNC milling. Furthermore, the 3D nature of SLA printing means that features of different height can be manufactured in one step, rather than the several lithography and etching steps which would be required if fabricating in silicon. This means that a wider spectrum of channel geometries can be achieved at reduced time, and thus cost of any manufactured inlays. A summary of the characteristics of different microfluidic manufacturing methods are shown in **Figure 1B** and a brief summary of bonding techniques is given in **Figure 1C**. As a demonstrator, we have designed and injection molded a microfluidic chip which was ultrasonically welded to a nanostructured plasmonic substrate. The integration of both parts forms a simple, fully injection molded biosensor.^[35] Furthermore, we have created a device to house liver organoids. This device consists of channels of varying height, and is sealed through ultrasonic welding to show how this fabrication method can be used for organ-on-a-chip applications.

2. Experimental Section

2.1. Inlay Fabrication

Inlays were designed using Solidworks computer aided design (CAD) software (Dassault Systèmes, France) and printed using a Form2 printer (Formlabs, US) in both Clear and High Temp resins (Formlabs proprietary resin formulations). This system

used an SLA process in which a photocurable resin was selectively patterned by a laser for each subsequent layer. Post printing, parts were removed from the build plate and any uncured resin was removed by washing in isopropyl alcohol while agitating for 10 min (Form Wash, Formlabs). Finally, all parts were allowed to dry at room temp before being cured under UV for 30 min at 60 °C (Form Cure, Formlabs). All inlays were printed with a layer height of 25 μm . Injection molding inlays were designed with dimensions of $24.7 \times 24.7 \times 8$ or $27.7 \times 77.7 \times 5$ mm to fit existing tooling. Inlays were designed using Solidworks computer aided design (CAD) software (Dassault Systèmes, France) and printed using a Form2 printer (Formlabs, US) in both Clear and High Temp resins (Formlabs proprietary resin formulations). This system uses an SLA process in which a photocurable resin is selectively patterned by a laser for each subsequent layer. Post printing, parts were removed from the build plate and any uncured resin was removed by washing in isopropyl alcohol while agitating for 10 min (Form Wash, Formlabs). Finally, all parts were allowed to dry at room temp before being cured under UV for 30 min at 60 °C.

2.2. Inlay Characterization

2.2.1. Surface Roughness

Surface roughness was measured using an Alicona Infinite Focus G4 optical microscope (Bruker, US) using a 10 \times objective (Olympus, Japan). Images were analyzed and surface roughness measurements obtained from Vision 64 Map Software (Bruker).

2.3. Optical Clarity

Optical clarity was measured using a 1951 USAF wheel pattern test target (Thorlabs, Germany). The target was placed on top of the chips and imaged with an EVOS 7000 (Thermo Fisher, US) microscope with a 10 \times objective (Olympus, Japan). To improve optical quality, chips were polished using Brasso (Reckitt Benckiser, UK) and a microfiber cloth.

2.3.1. Feature Dimensions

Inlays were sawed most of the way through from the back and then snapped so that a clean cross-section could be imaged. Cross-sectional images were captured using a Hitachi S4700 scanning electron microscope (SEM) (Japan) at 100 \times magnification. Molded polystyrene parts and sealed micro-channels were snapped after sawing most of the way through and dipping in liquid nitrogen to ensure a clean cleave. Parts were sputtered with gold/palladium prior to any imaging. Images were adjusted for contrast using ImageJ (National Institutes of Health and the Laboratory for Optical and Computational Instrumentation, US) and measured using a Python script.

2.4. Injection Molding

Polymer replicas were fabricated in polystyrene (PS) (1810 crystal polystyrene, Total Petrochemical and Refining, Belgium) using a

Victory 28 injection molding machine (Engel, Austria). PS was chosen as it is the primary material used for tissue culture devices in life-sciences.^[13] The polymer was heated to 260 °C and a shot volume of 4 cm³ was injected into the cavity (injection velocity = 1 cm³ s⁻¹). This was then cooled in the mold for 35 s (holding pressure = 800 bar) before the tool was opened slightly for a further 10 s to ensure the part was cooled sufficiently before releasing from the mold to avoid warping. As the cured resin is less thermally conductive than traditional injection molding materials (metals), a relatively long cooling time (35 s) was required to ensure the parts cooled to below the glass transition temperature (90 °C for PS) in the mold. This prevents any deformation that can occur when the part cools after it was ejected from the tool. After this time, the tool opened completely and the part was ejected. This molding process had not been optimized for reducing the cycle time. All devices had the sprue removed and inlets/outlets holes were drilled as required. A drilling speed of 100 rpm was used to prevent excessive heat build-up that would melt parts.

2.5. Ultrasonic Welding

During ultrasonic welding, parts were joined by vibrating the interface between them. This friction melts the polymer and the parts fuse together. Using energy directors referred to as weld-seams, this energy was localized to predefined regions, reducing heating and warping of the overall part. As such, triangular weld seams of varying dimensions were incorporated round the edge of the channel during the design. Channels were then sealed against a molded PS blank using a Standard 3000 welder (Rinco Ultrasonics, Switzerland) using travel differential mode (20%, 40%, 60%, 80%, and 100% of the weld seam height), and energy mode (5, 10, 15, 20, and 25 Ws) to determine the optimum settings. A hold time of 2 s was used throughout to allow the welds to cool before the parts were removed from the tool. Successful sealing was determined by filling the channel with food coloring (Morrisons, UK) and examining for leaks. Before sealing tests, parts were plasma treated in O₂ (80 W, 1 min) to increase their hydrophilicity. Sealed chips were then cleaved and their cross sections imaged (SEM) to determine the effect of weld seam dimensions on microchannel geometry.

2.6. Plasmonic Device Fabrication

Polystyrene templated plasmonic slides were fabricated according to a protocol adapted from Karimullah et al.^[40] In brief, a 40 \times 40 mm silicon wafer was ultrasonically cleaned and spun with Poly(methyl methacrylate) (PMMA). The nano-pattern, created in Tanner L-Edit (Siemens, Germany) was transferred to the surface using an EBPG 5200 electron beam lithography tool (Raith, Germany). The sample was then developed in a solution of methyl isobutyl ketone (MIBK)/isopropyl alcohol (IPA) in 1:2.5 by volume ratio. After development, 60 nm of nickel was deposited by thermal evaporation (MEB 550S Electron Beam Evaporator, Plassys, France). Acetone was used to wash away the remaining PMMA and overlying nickel, leaving only the nickel in the pattern defined during the lithography stage. The silicon was then etched to transfer the nickel pattern into the wafer (ICP RIE, Surface

Technology Systems, UK) to a depth of 240 nm. The nickel mask was then chemically stripped from the wafer. These features were then transferred into a master inlay and replicated via injection molding in PS according to the following protocol.^[41] Finally, the PS surface, patterned with ordered nanopillar array was plasmonically activated after thermal evaporation of a 100 nm Au thin film.

2.7. Plasmonic Measurements

Absorption measurements were taken on a USB2000 spectrometer (Ocean Optics, USA) with a 6 s integration time. Reference measurements were taken on a blank polystyrene slide coated with 100 nm gold film sealed with a microfluidic device for each liquid analyte. This reference was subtracted from the plasmonic data to give a true value of the plasmonic absorption of the devices.

2.8. Organoid-on-a-Chip

Channels with a cross section of $300 \times 300 \mu\text{m}$ with constriction at one end lowering the depth to $100 \mu\text{m}$ were molded from 3D printed inlays. Liver organoids were generated as described in references^[42,43] and pipetted into the channels before tubing was connected and media was either flowed through at a rate of $100 \mu\text{L h}^{-1}$ or left without flow. After 1, 3, or 7 days, the cells were washed with PBS and stained with a live dead stain (LIVE/DEAD Viability/Cytotoxicity Kit, for mammalian cells, Invitrogen, US) and imaged on a Zeiss LSM700 confocal microscope using Zen capture software.

3. Results and Discussion

3.1. Fabrication and Characterization of Micro-Channels in 3D Printed Inlays

Although there are a wide range of 3D printers and materials available, work here was focused on Formlabs printers and resins. The Form 2 printed used for this work only allows for the use of Formlabs resins (proprietary mixtures of methacrylic acid esters and a photo-initiator^[44]). Despite the proprietary nature of the resins, the resins and printer were used here as any variability between printers and homemade resins is eliminated.

Initially, Formlabs' High Temp resin was used to print inlays as it was thought that its high heat deflection temperature would make it more suitable for injection molding. This data is summarized in Table S1, Supporting Information. However, the High Temp resin proved too brittle to withstand the 800 bar pressure inside the tool leading to cracking of the inlay (Figure 2A). Interestingly, the standard, clear resin was able to withstand both the pressure and temperature of the molding cycle so was used for all further inlays. This despite the clear resin having a lower heat deflection temperature (S1). However, the higher elongation to failure illustrates that the clear resin was tougher and thus better suited to injection molding. Furthermore, the fidelity of the injection molding process was measured to investigate the durability

of the molds and is discussed in detail later. Figure 2B shows the clear resin intact after 500 shots.

For microfluidic applications, it is important for any fabrication process to give features of predictable cross sections and thus predictable fluid kinematics under flow. However, the default printer settings meant the inlay was printed at a different angle with each subsequent print, leading to variation in the profile and dimensions of the ridge. To analyze this effect, we printed straight ridges at a range of angles rotating in the θ (around the face of the inlay) and φ (around the side of the inlay so that the features face towards the print bed) directions as defined by Figure 2C where SEM images of the cross sections of these ridges can be seen. Here, the ridge printed at 0° in both the θ and φ directions have a symmetrical profile however, channels not running in the build direction will have a profile of that at $\theta = 90^\circ$ and $\varphi = 0^\circ$. This means this orientation is only useful for linear microfluidic channels. To address this, ridges printed facedown ($\varphi = 90^\circ$) exhibit a symmetrical profile and steep sidewalls and the profile is not influenced by the orientation of the channel on the part.

In a typical printing process, supports and a base are added by the slicing software used by the printer to create a normalized build plane on the build plate. This ensures that the exact position of the build plate is not required for the printing of each part and allows the resin to easily flow around the print, thus preventing a build-up of resin which might be cured by scattered light during printing. However, it was found that printing devices directly on the build plate without the base and supports not only cut down on print time, but also resulted in more reproducible parts. Additionally, the lack of supports meant that these did not need to be removed before molding thus cutting fabrication time even further.

In addition to predictable profiles, surface roughness measurements were taken of 3D printed inlays with no features on their surface to give an indication of the optical clarity of the molded parts. Surface roughness affects the transparency of the final devices so should ideally be as low as possible. Surface roughnesses of $Ra = 0.81 \pm 0.02 \mu\text{m}$, $Rq = 1.07 \pm 0.10 \mu\text{m}$, and $Rz = 4.97 \pm 0.49 \mu\text{m}$ were obtained (mean \pm standard deviation, $n = 3$) which is an order of magnitude smaller than similar 3D printed tooling for embossing described previously.^[20] However, as surface roughness can be misleading as an indicator of optical clarity, a resolution target was used to better understand the optical quality. Using this, chips were able to resolve 0.28 line pairs per millimeter (lp/mm) however, by polishing the inlay prior to molding, the chips could then resolve 128 lp/mm. Images of the target's smallest features through the unpolished chip is shown in Figure 2D and the polished chip in Figure 2E.

Alongside optical clarity and predictable profiles, accurate fabrication of channels with well-defined widths and heights is also of paramount importance when manufacturing microfluidic devices to predict fluid kinematics in the final device. As such, ridges of varying heights and widths were designed and printed with a 5° draft angle to ease the demolding, in accordance with good results from preliminary experiments, both in terms of demolding and linewidth consistency (Figure S1, Supporting Information). Additionally, control over the draft angle highlights another advantage of 3D printing as sloping features are difficult to fabricate with standard photolithography processes. SEM

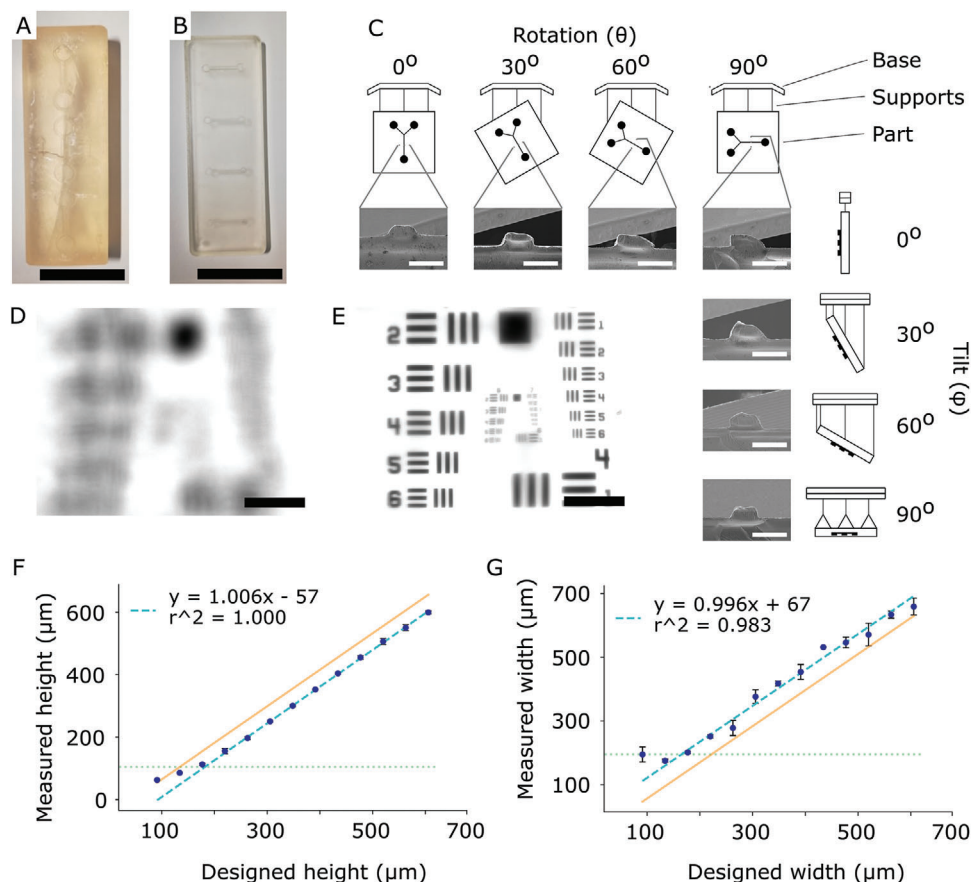


Figure 2. A) and B) show inlays post molding in the Formlabs high temp and clear resin, respectively. Cracks appeared in the high temp resin after 10 shots in the injection molding machine while the inlay made from the clear resin is intact after 500 shots. C) shows how the orientation of the print affects the cross-sectional profiles of the printed ridges. Printing facedown gives the most consistent profiles for all features printed on the inlay. D) and E) show images of the optical clarity target imaged through parts molded from unpolished and polished inlays, respectively. F) shows the measured heights versus designed heights for features 300 μm wide. Only points above 100 μm were used to determine best fit lines (linear regression, green dashed lines). Orange lines show the measured height = designed height. G) shows the measured widths versus designed widths for features 300 μm high. Best fit was taken from all points above 200 μm . All points are mean \pm standard deviation with $n = 3$. Scale bars = 25 mm for (A) and (B), 200 μm for (C), and 100 μm for (F) and (G).

micrographs were acquired and the cross sections measured were compared to the designed dimensions. The height of a channel was defined as the distance from the base of the part to the top of the ridge. The width was defined as the width at 50% of the full height to account for the sloped sidewalls and reduce any measurement ambiguity imposed by the ridges' corner radius.

The measurements for the heights of the ridges are shown in Figure 2F showing the heights of features 300 μm wide. The data for features 200 and 400 μm wide can be seen in Figures S2A and S2B, Supporting Information. This shows that, for a range of widths of the ridges, the heights are offset by a value of -59 ± 1.7 μm . This decrease in the height of a feature is likely due to an over curing of the resin designed to ensure robust printing. The slope of the best fit lines (least squares regression) shows that this systematic error can be compensated for by including this offset into the design of the feature.

The measured widths of the features printed at heights of 300 μm versus their designed widths are presented in Figure 2G. Again, the data for features 200 and 400 μm sizes can be seen in Figures S2C and S2D, Supporting Information. Similar to the

heights discussed above, the best fit lines of the lines regions of the plots show r^2 values ≈ 1 and an offset of 66 ± 3.2 μm . This discrepancy in the measured versus designed widths is because as each subsequent layer is cured by the laser in the printer, this light is scattered and any uncured resin that is still coating features in previous layers is exposed. Hence the features are wider at the bottom than the top. Combining this with the offset acquired from the height data above, a general rule for printing ridges is to overcompensate for the height by 59 μm and undercompensate for the width by 66 μm . This was found to give accurate and reproducible features for all subsequent experiments and devices. It is also worth mentioning that within the range of widths and heights studied here, aspect ratio had no effect on the measured dimensions of the features. Thus, the printing process is not limited by the aspect ratio.

To further characterize the capabilities of this fabrication process, ridges were printed at different spacings to determine the resolution of the printer—that is, the minimum distance between two features that still give two distinct features of the designed height, with no material filling in the gap between them.

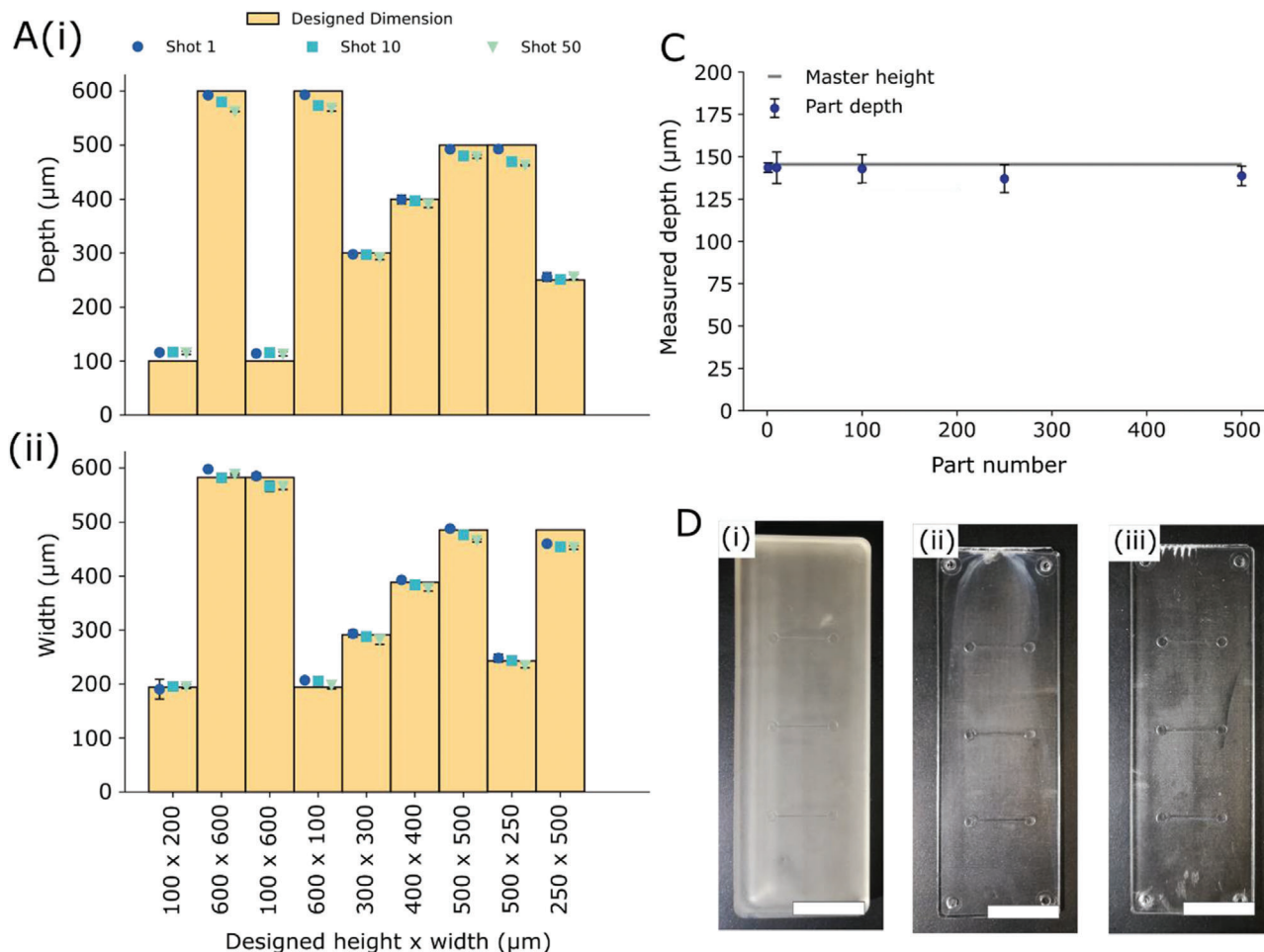


Figure 3. A) (i) shows the designed heights of features (orange bars) and the depths of the channels molded after the 1st, 10th, and 50th shots for channels of different geometries. Here it can be seen that for the shorter channels, replication of a desired feature is good over a high number of shots while the deeper channels (400 µm and above) lose their depth with subsequent shots. (ii) shows the same data but for the widths of the channels. B) shows the durability of a 3D printed inlay over a production run of 500 parts where the dimensions of the 500th part are still within error compared to the inlay. C) shows photographs of the inlay, the 1st, and the 500th part in (i)–(iii) respectively. Scales bars = 15 mm.

This was achieved by measuring the heights of the features at different spacings where a ridge of full, designed height indicates a fully resolved feature. This data is shown in Figure S2E–G, Supporting Information, which indicates the heights of features, normalized to their various designed heights, at widths 200, 400, and 600 µm, respectively. The orange areas illustrate the distances for which the ridges were fully resolved (greater than 400 µm for the 200 and 400 µm wide features and greater than 600 µm for the 600 µm wide features).

3.2. Inlay Durability for Multiple Injection Molding Cycles

The injection molding process involves high temperatures and pressures (260 °C and 800 bar) which can lead to wear and damage to inlays used for molding. As such, it was important to test the accuracy and reproducibility of the micro-channels molded from our 3D printed inlays as well as the durability of the inlays themselves. A series of ridges of varying width, height and aspect ratio were printed at desired dimensions accounting for the off-

sets and spacings determined above. The height and width of the channels formed on the thermoplastic replicas were then measured and compared to the designed dimensions. **Figures 3A(i)** and **A(ii)** show how the replication of the height and width varies over 50 shots, respectively.

Here it can be seen that shallower channels showed very good reproducibility over the full production run while the taller channels, particularly those over 500 µm, showed a reduction in height of 30 µm with successive shots. In terms of the widths, a small reduction in the width of the channels can be observed over most of the designs with each shot, however, this is most apparent in the higher aspect ratio channels. Shorter and lower aspect ratio channels show excellent reproducibility over the production run. To further validate this an inlay was printed with channels 146 µm deep and 500 parts were molded from it. The 1st, 10th, 100th, 250th, and 500th part were measured and this data is shown in Figure 3B. Here it can be seen that even after 500 parts have been molded, the channel height is still within error of the master dimensions showing that 3D printed inlays are durable for at least 500 parts. Photographs of the master, the 1st part and the 500th

part are shown in Figures 3C(i) and c(iii), respectively. It is also worth mentioning that the injection and the cooling of the polymer in the tool have not been optimized but provides adequate replication for microfluidic channels over an acceptable range of dimensions. As such, the molding process could be refined through modelling and further experimentation should a wider range of geometries be required.

3.3. Impact of 3D Design and Ultrasonic Welding on Sealing

In the case of PDMS, bonding to other materials can be achieved with relative ease; the most common methods involving sealing against itself or against a glass substrate. This is possible because the elasticity of PDMS lets it conform to a surface and provide a moderate seal.^[45] This sealing can be enhanced by first plasma treating the elastomer when a higher pressure seal is required.^[46] However, bonding of inelastic thermoplastics is not so trivial. Thermal sealing involves heating the two parts and holding them together under pressure to allow the parts to fuse together. However, the need for a long cooling stage means that this method is not viable for high throughput applications. Furthermore, the fact that the whole part needs to be heated can lead to deformation within the channels.

Ultrasonic welding is one of the most common thermoplastic bonding processes used in industry due to its rapid, easy to automate, and cheap nature, as well as the fact it requires no additional materials for the fusion of parts. As such, ultrasonic welding complements the injection molding process for high-throughput, rapid manufacture of devices. During ultrasonic welding, it is beneficial to use energy directors (referred to as weld seams). These structures act to focus the welding energy to a small, localized region of the device and prevent excessive deformation of the parts due to heating. Once in contact, the sonotrode exerts pressure and ultrasonic vibrations onto the two parts which heats and melts the weld seam, thus fusing the two parts together. By having the seam encircle the channel, a hermetic seal is formed during the fusion of the parts. Typically, these weld seams need to have a triangular profile which is difficult to fabricate with traditional silicon micromachining protocols. However, with 3D printing, complex 3D shapes can be incorporated into the device with ease, thus reducing the fabrication time while simultaneously allowing for geometries that would be extremely challenging to manufacture using traditional advanced manufacturing methods.

First, it was important to determine the smallest weld seam structures that could be achieved through 3D printing. Smaller weld seams will have a smaller effect on the geometry and the performance of a microchannel however, too small, and there will not be enough material to seal the chip. The lower weld seam size limit was determined by printing a series of troughs (that would become ridges in the molded part) of different depths (100 and 200 μm) and widths (200–700 μm), cleaving the part and imaging the cross-section before measuring and comparing to the designed geometries. Further information on the dimensions of the printed features can be found in Figure S3A(i), Supporting Information. For narrower channels, the printer was not able to realize the designed shape as the resolution was not high enough. This resulted in features filling in which can be seen in Figure 4A.

However, for wider features, this filling in was less of an issue and the troughs were able to be printed (Figure 4B). By measuring and comparing the widths and heights of these troughs to the designed dimensions, the lower feature size limit could be determined. Figures 4C and D show the widths and depths of features 100 and 200 μm deep, respectively. These results show that the narrowest trough feature that can be reliably printed was 350 μm wide.

Next, in order to achieve the desired triangular shape of the features, a series of troughs was printed with a range of sidewall angles. This was done in order to determine the most triangular channel that could be printed. The shape of these features with the side wall angle is shown in Figure S3A(ii), Supporting Information, with the ideal profile shown in Figure S3A(iii), Supporting Information. Figures 4E and F show the measured depths of troughs designed to be 350 μm wide and 100 and 200 μm deep, respectively. This illustrates that for 100 μm deep troughs, the side wall angle can be increased to 15° while it can only be increased to 2° for the 200 μm deep ones. Considering the design requirements set out above, channels were designed to have weld seams encircling them with dimension of either height = 100 μm , width = 350 μm , and sidewall = 15° or height = 200 μm , width = 350 μm , and sidewall = 2°. These parts were then molded and plasma treated, after which inlet/outlet holes were drilled.

To determine the optimum welding parameters for these weld seams, two different operation modes on the ultrasonic welding machine were considered: travel differential, and energy mode. In travel differential mode, the sonotrode moves a predefined distance while vibrating to fuse the parts, while in energy mode, the sonotrode vibrates until a certain energy has been transferred to the parts. Using a travel differential of 20%, 40%, 60%, 80% and 100% of the weld seam height, 10 chips were sealed at each setting and the sealing success was determined by filling the channels with dye and examining for leaks. As both parts were plasma treated prior to sealing (hydrophilic surfaces), any leak from the channel meant that fluid easily could escape and was almost instantly visible to the eye. The same was done in energy mode using energies of 5, 10, 15, 20, and 25 Ws. The sealing success of the two weld seam designs is shown in Figure 4G. Here it can be seen that the 200 μm seams sealed more effectively than the 100 μm ones, and that energy mode was far more successful in sealing the chips than travel differential mode. No 100 μm seams sealed in travel differential mode while energy mode had a 100% success rate for the 200 μm seams at energies over 10 Ws. However, the 100 μm seams could reliably seal in energy mode at 25 Ws.

As ultrasonic welding involves the melting of weld seams, the process does mean that the resulting microchannel includes the added height of these structures. As such, it was important to determine how much height is added so that this can be compensated for in the design. Chips were sealed using the parameters described above before being cleaved and their cross sections imaged and measured. Added height was defined as the height from the bulk of the chip material to the foil used to seal. Figure 4H shows the added heights for all the designs and welding parameters that gave a sealing rate of above 90%. This shows that, for the 200 μm seams, the more energy used to weld, the less height was added to the final channel. It was thought that using a smaller weld seam would result in less overall added height however, the

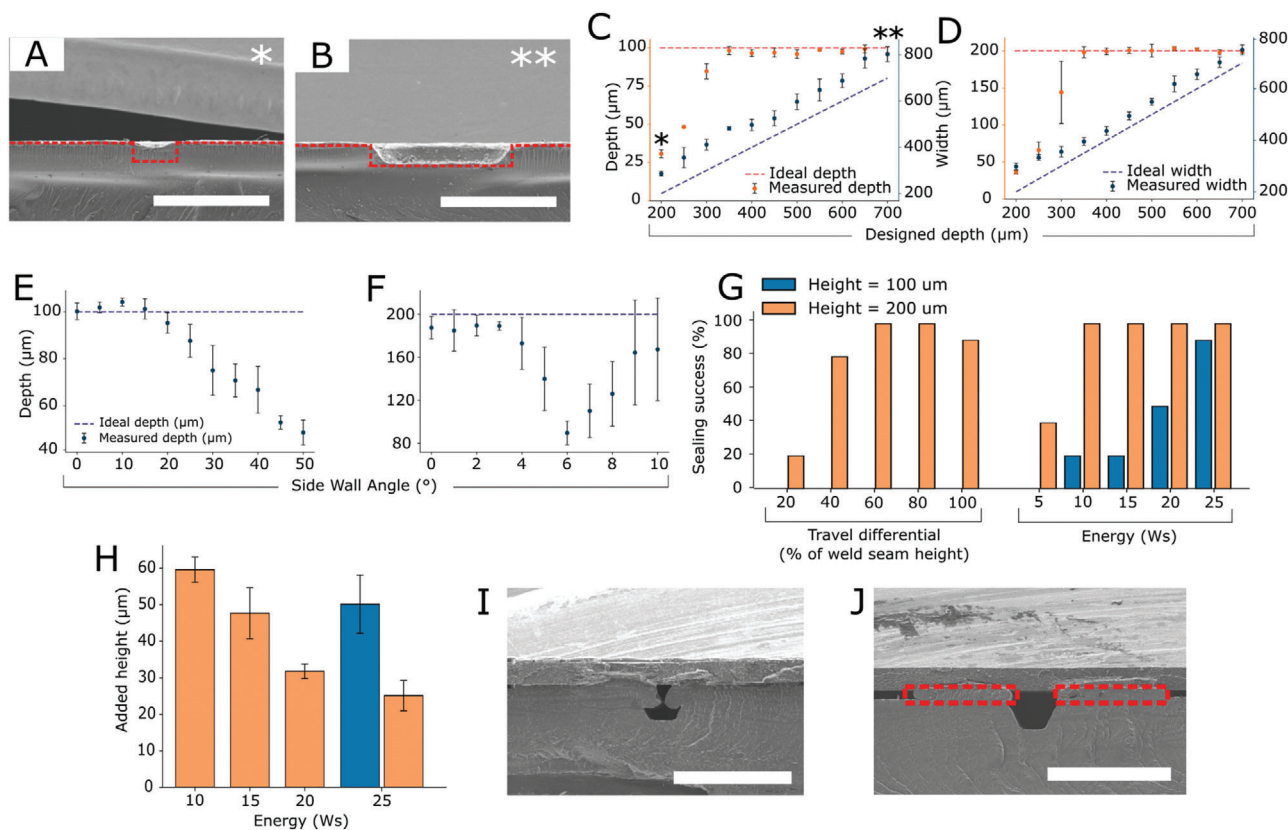


Figure 4. A) and B) show printed trough with designed dimensions of $200 \times 100 \mu\text{m}$ (width \times depth) and $700 \times 200 \mu\text{m}$, respectively. Red dotted lines show the designed shape of the trough. Filling in of the feature can be observed in the smaller channel, while the larger one is better realized. C) and D) show how the designed and the measured dimensions of these features differed from one another for features 100 and 200 μm deep, respectively. With the full depth of the features only being realized once the width is above 350 μm . The effect on the sidewall angle on the depth of the channels is shown in E). This shows how the side wall angle of these features affects the depth of a 100 μm trough. F) shows the same as E) but for a 200 μm trough. The sealing success of different welding parameters and weld seam designs is shown in G) and the added heights of the successfully sealed channels are shown in H). Finally, I) and J) show cross sectional images of sealed channels where the weld seams were placed adjacent to the channels and offset by 150 μm , respectively. Red dotted boxes show the weld seams and how they fit in the final channel in J). Scale bars in (A) and (B) = 500 μm and 1 mm in (I) and (J).

100 μm seam gave an added height of 50 μm compared to 28 μm for the 200 μm one. It is assumed that this is down to the profile of the 200 μm seam being more pointed, thus allowing for a more efficient transfer of energy, and more of the plastic melting and fusing. It was also noted during this experiment that material from the weld seams was flowing into the microchannels during welding (Figure 4I). Finally, it was hypothesized that placing the seams adjacent to the channels would give the best channel profile once sealed, but this was not the case (Figure S3B(i), Supporting Information). Fortunately, these defects could be compensated for, by moving the weld seams 150 μm back from the edge of the channel (Figure 4J) (designs shown in Figure S3B(ii), Supporting Information).

3.4. Demonstration of an Injection Molded Plasmonic Sensor

To demonstrate the method of using 3D printed inlays to mold microfluidic parts, we created a simple plasmonic biosensor. Integrating sensors into microfluidic devices increases their attractiveness for biomedical applications and keeps them in line with

the tenets that were first laid out for microfluidics.^[47] Here we use the above method of ultrasonic welding to seal a microfluidic device to an injection molded nanopatterned polystyrene slide coated with 100 nm of gold. The gold nanostructures can enhance localized surface plasmon resonance (LSPR), thus creating a fully injection molded plasmonically active sensor. A photograph of such a device is shown in Figure 5A with an SEM of the channel and nanopattern shown in Figures 5B and C. Localized surface plasmon resonance (LSPR) has been widely used in biomedical and chemical sensing applications and works as follows. The conducting electrons of the metal nanostructures, spatially confined to the interface of the nanoscale object, create characteristic resonant oscillation upon stimulation with incident light. This resonance causes the metal nanostructures to absorb light at a specific wavelength dependant on the period of the oscillation. As it is sensitive to changes in the local dielectric environment, using an array of nanopillars (130 nm diameter, 190 nm pitch) we were able to detect the difference in absorption of different analytes (water and 20%, 40%, 60%, 80% glucose solutions). These absorption spectra are shown in Figure 5D with all measurements recorded on the same device. This ability to easily incorporate a

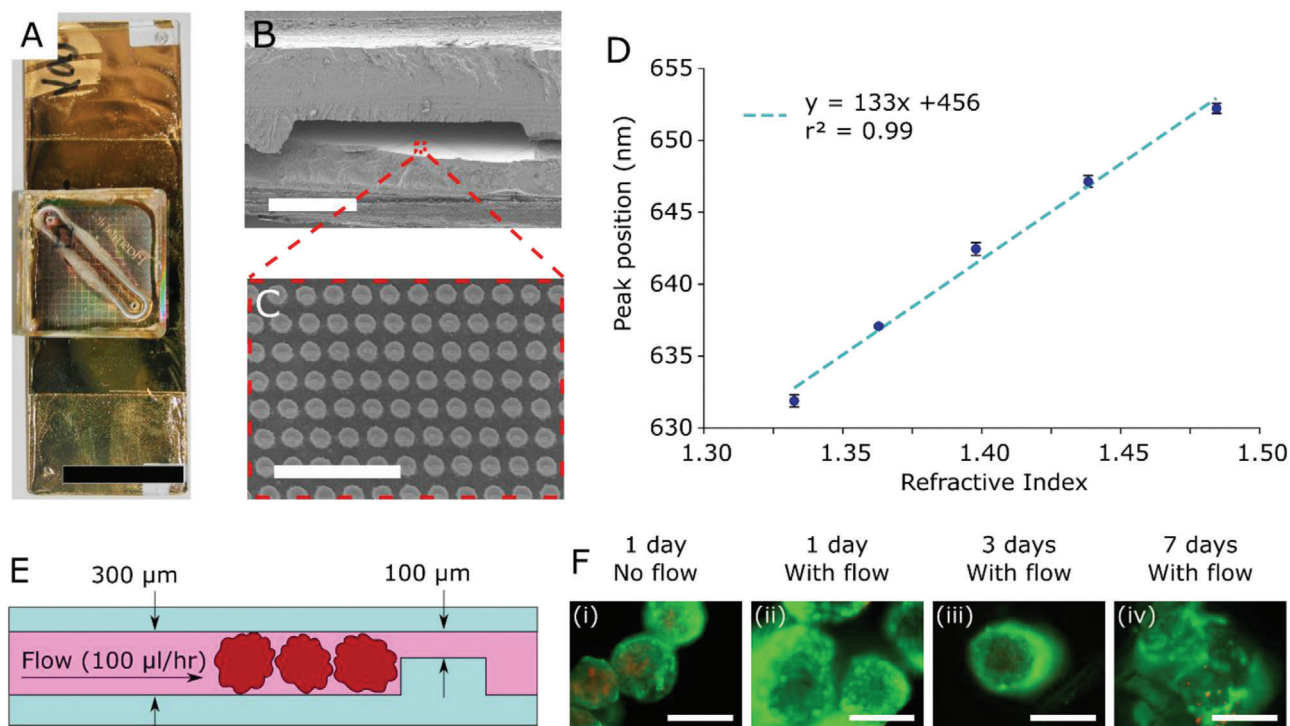


Figure 5. A) shows a photograph of an assembled microfluidic plasmonic device. B) shows an SEM of a cross section of the channel, and C) shows the nano-pattern on the base of the channel. D) shows that how by changing the refractive index of media in the microchannel (0%, 20%, 40%, 60%, and 80% glucose solutions), the resonance peak shifts. E) shows a schematic of the organoid-on-a-chip device while F) shows the cell viability after 1 day without and with flow, 3 days, and 7 days in the chip in (i)–(iv), respectively. Green = calcein (alive cells) while red shows propidium iodide (dead cells). Scale bars are 25 mm in (A), 1 mm in (B), 1 μm in (C), and 200 μm in (F).

well understood sensing technique into a microchannel of any desired geometry is an attractive property for microfluidic fabrication. As discussed by Manz et al, detection of analytes is one of the key applications of microfluidics^[47] and also ensures that minimal equipment is required for the operation of chips meaning that lab-on-a-chip devices can be created as opposed to a chip-in-a-lab.^[48]

3.5. Organoid-on-a-Chip

To further demonstrate the applications of injection molded microfluidics from 3D printed inlays, we created a device capable of housing liver organoids and maintaining their viability for multiple days. Organoids are 3D structures of cells composed of the different cell types required to make up an organ. In the case of liver cells, the organoids were composed of hepatocytes, cholangiocytes, stellate cells, kupffer cells, and endothelial cells. Organoids are organotypic in vitro models that capture the complexity and physiology of the organ and organ systems within the body and are thus an area of great interest within the organ-on-a-chip community. Furthermore, the size of the organoids used here (100–300 μm in diameter), meant that any devices manufactured have to also be on this length scale which makes injection molded parts from 3D printed inlays all the more appealing. Here, a simple 300 \times 300 μm fluidic channel connecting an inlet

and an outlet were fabricated. However, the channel had a constriction at one end lowering the depth of the channel to 100 μm . This constriction meant that organoids got trapped and held in the chip, but media was still able to flow around the cells to supply nutrients. Again, this complex 2.5D geometry would be very difficult to fabricate using other manufacturing methods, but with 3D printing, it is a simple, 1-step process. A schematic of this chip is shown in Figure 5E. Once the organoids were loaded into the chips, tubing was connected and media was supplied to the chips from a syringe pump at a rate of 100 $\mu\text{L h}^{-1}$. Cells in different chips were stained after 1, 3, and 7 days with an additional chip stained with a live dead stain after 1 day but with no media (no flow) supply acting as a negative control. These fluorescent images can be seen in Figure 5F (i)–(iv) showing the organoids after 1 day with no flow, 1, 3, and 7 days with flow, respectively). Here it can be seen that after one day with no flow of media, the cells in the organoids are predominantly alive however, there is a higher number of dead cells compared to the others. The organoids supplied with flowing media showed a minimal number of dead cells, showing that the organoids stayed healthy after seven days in the chip. This ability to maintain cell viability for prolonged periods of time highlights the attractiveness of polystyrene microfluidic chips, and the fact that such a chip was simple and cost effective to manufacture at the length scales required, show a usable example of microfluidic chips molded from 3D printed inlays.

4. Conclusion

We have demonstrated a unique approach of manufacturing polystyrene microfluidic devices via injection molding from a 3D printed master. Channels as small as $100 \times 200 \mu\text{m}$ could be fabricated. Although larger than microfluidic devices fabricated by photolithography, these dimensions are currently limited only by the 3D printer and are expected to reduce as printers become more capable. Moreover, with the emergence of organoid technologies, these higher length scales will become the required dimensions for many organoid-on-a-chip devices. In summary, accurate dimensions of the features could be realized by compensation at the design stage. Designing features to be $59 \mu\text{m}$ taller, $66 \mu\text{m}$ narrower, and with a draft angle of 5° , channels of a desired geometry can be achieved if they are placed more than $500 \mu\text{m}$ apart. Furthermore, by ensuring in the aspect ratio of a channel is under 2:1, and the overall height is under $500 \mu\text{m}$, the inlays can produce at least 50 identical parts before gradual deterioration of the inlays was observed. Finally, the design of energy directors for ultrasonic welding was optimized showing that features as small as $350 \times 100 \mu\text{m}$ could be printed and used to seal the device, however, more reliable sealing was seen with larger energy directors ($350 \times 200 \mu\text{m}$).

It is important to mention the time frame of this fabrication process. Allowing 1 h for the design of a device, it takes 2.5 h to print, wash, and cure the inlay, 2 h to prepare the injection molding machine and mold 50 parts, and 30 min to drill inlets/outlets and seal the chips. This represents a total time of 6 h, meaning that devices can be designed, fabricated, and tested within one working day. This allows for multiple iterations of a device to be tested rapidly before a final design is settled on. Furthermore, the ability to mold over 500 parts shows how such a technique can be used in semi-industrial applications.

The use of ultrasonic welding allowed not only for leak-free sealing of molded parts, but also the incorporation of functionally patterned, plasmonically active plastic parts (with metal coatings) to create a microfluidic biosensor capable of specific, quantitative measurements with applications in academic and commercial microfluidic and sensing practices. Additionally, the fact that complex biological structures could be maintained within the chips highlights how these chips could be used in organ-on-a-chip applications with built in bio-sensing capabilities.

In summary, this novel approach combines low cost, rapid-prototyping, and high-throughput, industrial scale manufacture in a manner that is unparalleled by existing processes.

Supporting Information

Supporting Information is available from the Wiley Online Library or from the author.

Acknowledgements

This work was supported by the Engineering and Physical Sciences Research Council (EPSRC) grant EP/N509668/1 and by the Research Council of Norway through its Centres of Excellence funding scheme, project number 262613. This study was partially funded by a European Research Council Consolidator Award "FAKIR", reference 648892. This research was funded as part of the North West Centre for Advanced Manufacturing. The

North West Centre for Advanced Manufacturing (NWCAM) project is supported by the European Union's INTERREG VA Programme, managed by the Special EU Programmes Body (SEUPB). The views and opinions in this document do not necessarily reflect those of the European Commission or the Special EU Programmes Body (SEUPB). If you would like further information about NW CAM please contact the lead partner, Catalyst, for details

Conflict of Interest

The authors declare no conflict of interest.

Data Availability Statement

The data that support the findings of this study are available from the corresponding author upon reasonable request.

Keywords

injection molding, microfluidics, organ-on-a-chip, plasmonics, sealing

Received: June 24, 2021
Revised: September 6, 2021
Published online: October 13, 2021

- [1] H.-P. Chou, C. Spence, A. Scherer, S. Quake, *Proc. Natl. Acad. Sci. USA* **1999**, *96*, 11.
- [2] A. Bernard, B. Michel, E. M. Delamarche, *Anal. Chem.* **2001**, *73*, 8.
- [3] S. K. Sia, G. M. Whitesides, *Electrophoresis* **2003**, *24*, 3563.
- [4] D. J. Beebe, G. A. Mensing, G. M. Walker, *Annu. Rev. Biomed. Eng.* **2002**, *4*, 261.
- [5] G. M. Whitesides, *Nature* **2006**, *442*, 368.
- [6] N. Convery, N. Gadegaard, *Micro Nano Eng.* **2019**, *2*, 76.
- [7] B. J. van Meer, H. de Vries, K. S. A. Firth, J. van Weerd, L. G. J. Tertoolen, H. B. J. Karperien, P. Jonkheijm, C. Denning, A. P. IJzerman, C. L. Mummery, *Biochem. Biophys. Res. Commun.* **2017**, *482*, 323.
- [8] K. J. Regehr, M. Domenech, J. T. Koepsel, K. C. Carver, S. J. Ellison-Zelski, W. L. Murphy, L. A. Schuler, E. T. Alarid, D. J. Beebe, *Lab Chip* **2009**, *9*, 2132.
- [9] T. Gervais, J. El-Ali, A. Günther, K. F. Jensen, *Lab Chip* **2006**, *6*, 500.
- [10] D. T. Eddington, J. P. Puccinelli, D. J. Beebe, *Sens. Actuators B: Chem.* **2006**, *114*, 170.
- [11] E. Berthier, J. Warrick, H. Yu, D. J. Beebe, *Lab Chip* **2008**, *8*, 852.
- [12] C. D. Chin, V. Linder, S. K. Sia, *Lab Chip* **2012**, *12*, 2118.
- [13] E. Berthier, E. W. K. Young, D. Beebe, *Lab Chip* **2012**, *12*, 1224.
- [14] D. J. Guckenberger, T. E. De Groot, A. M. D. Wan, D. J. Beebe, E. W. K. Young, *Lab Chip* **2015**, *15*, 2364.
- [15] M. E. Wilson, N. Kota, Y. Kim, Y. Wang, D. B. Stolz, P. R. LeDuc, O. B. Ozdoganlar, *Lab Chip* **2011**, *11*, 1550.
- [16] C. E. Owens, A. J. Hart, *Lab Chip* **2018**, *18*, 890.
- [17] H. Klank, J. P. Kutter, O. Geschke, *Lab Chip* **2002**, *2*, 242.
- [18] A. K. Au, W. Lee, A. Folch, *Lab Chip* **2014**, *14*, 1294.
- [19] P. J. Kitson, M. H. Rosnes, V. Sans, V. Dragone, L. Cronin, *Lab Chip* **2012**, *12*, 3267.
- [20] T. Y. Lin, T. Do, P. Kwon, P. B. Lillehoj, *Lab Chip* **2017**, *17*, 241.
- [21] M. B. Esch, S. Kapur, G. Irizarry, V. Genova, *Lab Chip* **2003**, *3*, 121.
- [22] S. Miserere, G. Mottet, V. Taniga, S. Descroix, J. L. Viovy, L. Malaquin, *Lab Chip* **2012**, *12*, 1849.
- [23] L. J. Kricka, P. Fortina, N. J. Panaro, P. Wilding, G. Alonso-Arnigo, H. Becker, *Lab Chip* **2002**, *2*, 1.

- [24] M. Matschuk, N. B. Larsen, *J. Micromech. Microeng.* **2013**, *23*, 25003.
- [25] N. Gadegaard, S. Mosler, N. B. Larsen, *Macromol. Mater. Eng.* **2003**, *288*, 76.
- [26] D. A. Mair, E. Geiger, A. P. Pisano, J. M. J. Fréchet, F. Svec, *Lab Chip* **2006**, *6*, 1346.
- [27] L. Yu, C. G. Koh, L. J. Lee, K. W. Koelling, M. J. Madou, *Polym. Eng. Sci.* **2002**, *42*, 871.
- [28] J. Giboz, T. Copponnex, P. Mélé, *J. Micromech. Microeng.* **2007**, *17*, R96.
- [29] D. Macintyre, S. Thoms, *Microelectronic Engineering* **1998**, *41-42*, 211.
- [30] J. Zhao, R. Ong, G. Chen, Y. K. Juay, F. L. Ng, M. W. Lee, C. H. Kua Int. Conf. Nanochannels, Microchannels Minichannels, Proc., 6th, Pts A and B, ASME, New York 2008, 1187–1194.
- [31] S.-H. Yoon, P. Palanisamy, P. Padmanabha, J. L. Mead, C. M. F. Barry, *Volume 12 Micro Nano Systems, Parts A and B* **2009**, *12*, 545.
- [32] T. S. Hansen, D. Selmececi, N. B. Larsen, *J. Micromech. Microeng.* **2010**, *20*, 015020.
- [33] S. W. Park, W. I. Lee, S. N. Moon, Y.-E. Yoo, Y. H. Cho, *Express Poly. Lett.* **2011**, *5*, 950.
- [34] N. Zhang, C. J. Byrne, D. J. Browne, M. D. Gilchrist, *Mater. Today* **2012**, *15*, 216.
- [35] J. M. Stormonth-Darling, N. Gadegaard, *Macromol. Mater. Eng.* **2012**, *297*, 1075.
- [36] J. Steigert, S. Haeberle, T. Brenner, C. Muller, C. P. Steinert, P. Koltay, N. Gottschlich, H. Reinecke, J. Ruhe, R. Zengerle, J. Ducre, *J. Micromech. Microeng.* **2007**, *17*, 333.
- [37] K. Kamei, Y. Mashimo, Y. Koyama, C. Fockenber, M. Nakashima, M. Nakajima, J. Li, Y. Chen, *Biomed. Microdevices* **2015**, *17*, 36.
- [38] T. Finkbeiner, H. L. Soergel, M. P. Koschitzky, R. Ahrens, A. E. Guber, *J. Micromech. Microeng.* **2019**, *29*, 065011.
- [39] K. Kistrup, C. E. Poulsen, M. F. Hansen, A. Wolff, *Lab Chip* **2015**, *15*, 1998.
- [40] A. S. Karimullah, C. Jack, R. Tullius, V. M. Rotello, G. Cooke, N. Gadegaard, L. D. Barron, M. Kadodwala, *Adv. Mater.* **2015**, *27*, 5610.
- [41] A. Hamilton, J. Perris, N. Convery, D. M. Mulvihill, N. Gadegaard, *Macromol. Mater. Eng.* **2021**, *306*, 2100223.
- [42] S. P. Harrison, R. Siller, Y. Tanaka, Y. Xiang, B. Patterson, H. Kempf, E. Melum, K. S. Åsrud, M. E. Chollet, E. Andersen, P. M. Sandset, S. Baumgarten, F. Bonanini, D. Kurek, S. Mathapati, R. Almaas, K. Sharma, S. R. Wilson, F. S. Skottvoll, I. C. Boger, I. L. Bogen, T. A. Nyman, J. J. Wu, A. Bezrouk, D. Cizkova, J. Mokry, R. Zweigerdt, I.-H. Park, G. J. Sullivan, *bioRxiv* **2020**, 2020.12.02.406835.
- [43] R. Siller, S. Greenhough, E. Naumovska, G. J. Sullivan, *Stem Cell Rep.* **2015**, *4*, 939.
- [44] Formlabs. Clear Resin SDS., ASME, New York **2016**.
- [45] J. C. McDonald, D. C. Duffy, J. R. Anderson, D. T. Chiu, H. Wu, O. J. Schueller, G. M. Whitesides, *Electrophoresis* **2000**, *21*, 27.
- [46] M. A. Unger, H.-P. Chou, T. Thorsen, A. Scherer, S. R. Quake, *Science* **2000**, *288*, 113.
- [47] A. Manz, N. Graber, H. M. Widmer, *Sens. Actuators B: Chem.* **1990**, *1*, 244.
- [48] M. I. Mohammed, S. Haswell, I. Gibson, *Procedia Technol.* **2015**, *20*, 54.